Online Cross-Sectional Monitoring of a Swirling Flame Using TDLAS Tomography

Online Cross-Sectional Monitoring of a Swirling Flame Using TDLAS Tomography

Chang Liu, Zhang Cao, *Member, IEEE*, Yuzhen Lin, Lijun Xu, *Senior Member, IEEE*, and Hugh McCann, *Senior Member, IEEE*

***Abstract*— The purpose of this paper is to monitor the dynamic cross-sectional behavior of swirling flames using the tunable diode laser absorption spectroscopy (TDLAS) tomographic system. The newly developed online and highly spatially resolved imaging system based on TDLAS tomography was employed to monitor and reveal directly the reaction process in the swirling flame by reconstructing the 2-D distributions of temperature and H_2O concentration over a cross section of the flame. The system was demonstrated to be capable of capturing the temperature distribution accurately and inferring the thermal expansion over the cross section of interest in the swirling flame generated by a model swirl injector operating in partially premixed combustion mode. As the equivalence ratio was decreased, thermal oscillations extracted from the real-time 2-D reconstructions were used to infer the instability of the swirling flame. Furthermore, the developed system was applied to capture dynamically the process of blowout of the swirling flame, illustrating that the system can provide firsthand and reliable visual data to help prevent the flame from lean blowout (LBO). This paper reports the first experimental observation of the dynamic cross-sectional behavior of the swirling flame, enabled by the high spatial and temporal resolutions provided by the TDLAS tomographic imaging system. The developed system can help better understand the LBO mechanism so as to improve the performance of low-emission gas turbine combustors.**

***Index Terms*— Lean blowout (LBO), species concentrations, swirling flame, temperature, tomography, tunable diode laser absorption spectroscopy (TDLAS).**

Manuscript received July 26, 2017; revised October 12, 2017; accepted November 08, 2017. This work was supported in part by the National Science Foundation of China under Grant 61327011, Grant 613111201, and Grant 61620106004, in part by the Program for Changjiang Scholars and Innovative Research Team in University under Grant IRT1203, and in part by the U.K. Engineering and Physical Sciences Research Council via Platform under Grant EP/P001661/1. The Associate Editor coordinating the review process was Dr. Yong Yan. *(Corresponding author: Lijun Xu.)*

C. Liu is with the Ministry of Education's Key Laboratory of Precision Opto-mechatronics Technology, School of Instrument Science and Opto-Electronic Engineering, Beihang University, Beijing 100191, China, and also with the School of Engineering, The University of Edinburgh, Edinburgh EH9 3JL, U.K.

Z. Cao and L. Xu are with the Ministry of Education's Key Laboratory of Precision Opto-mechatronics Technology, School of Instrument Science and Opto-Electronic Engineering, Beihang University, Beijing 100191, China (e-mail: lijunxu@buaa.edu.cn).

Y. Lin is with the School of Energy and Power Engineering, Beihang University, Beijing 100191, China.

H. McCann is with the School of Engineering, The University of Edinburgh, Edinburgh EH9 3FB, U.K.

Color versions of one or more of the figures in this paper are available online at http://ieeexplore.ieee.org.

Digital Object Identifier 10.1109/TIM.2018.2799098

I. Introduction

RECENT years have seen increasingly strict regulation of pollutant emissions produced by combustion processes in gas turbines [1]. These pollutants cause serious problems concerning the environment and human health. To realize cleaner and more environmentally friendly power generation, various efforts have been made by employing the lean combustion technology [2], [3]. As low fuel/air equivalence ratios are maintained all over the reactive flow field, the lean combustion is generally characterized by low flame temperature, which suppresses the formation of thermal NO_x to a large extent. In addition, the lowered temperature increases the reliability and lifetime of engine components and thus reduces the maintenance requirement of gas turbines.

Swirl injectors are extensively employed to realize lean combustion in practical combustion processes. In a typical swirl injector, the flow is deflected by an array of vanes, which provide the desired flow pattern and fuel/air distribution [2], [4]. The swirling flame enables high-energy conversion in a small volume and exhibits good ignition and stabilization behavior over a wide operating range. Understanding the reaction mechanism of the swirling flame is important to optimize the structure of the swirl injector. Furthermore, the risk of a lean blowout (LBO) event is dramatically increased if the combustion condition of the swirling flame is close to the LBO limit [5]–[7]. In particular, LBO poses a significant safety hazard when occurring in aircraft engines and requires an expensive shutdown and restart procedure in land-based engines for power generation. To avoid LBO, combustors can be operated with a wide safety margin above the uncertain LBO limit (e.g., higher equivalence ratio) [8]. However, enhanced engine performance and reduction of NO_x emission will require a narrower LBO safety margin. For this purpose, *in situ* and real-time active control mechanisms are required to operate low-emission gas turbine combustors safely and reliably. An important part of the active control mechanisms is providing an accurate monitoring technique for the swirling flame with meaningful control variables.

As key parameters of the combustion processes, temperature and species concentrations have great potential for use as control variables in physics-based control strategies. In recent years, nonintrusive laser-based diagnostic technologies have been applied to sensitive measurement of the temperature and species concentrations of swirling flames [9]. These technologies mainly include laser Raman spectroscopy (LRS) [10], coherent anti-Stokes Raman scattering (CARS) [11], [12],

planar laser-induced fluorescence (PLIF) [13], [14], and tunable diode laser absorption spectroscopy (TDLAS) [15], [16]. Many researches have been carried out to measure point-wise, path-averaged, and 1-D temperature and species concentrations, which can be used to infer the instability of the swirling flame and pollutant emissions. For instance, Roy *et al.* [11] demonstrated the applicability of single-shot CARS in measuring the point-wise temperature and relative concentrations of N_2 and CO_2 in the exhaust stream of a swirling flame. Li *et al.* [17] developed a line-of-sight TDLAS sensor to monitor the temperature oscillations in propane/air flames in a swirl-stabilized combustor. Stopper *et al.* [18] employed 1-D LRS to measure the temperature and the concentration of major species of the flame generated by a model swirl burner.

The 2-D spatially resolved measurements of temperature and species concentrations will not only help to better understand the underlying LBO mechanisms as the equivalence ratio is reduced but also to validate and optimize numerical combustion simulation models which then can be applied to simulate the behavior of technical combustors. The PLIF technique shows significant applicability to image 2-D distributions of temperature and species concentrations of the combustion fields with high spatial resolution. For instance, Meier *et al.* [19] applied a two-line PLIF system for the first time to measure the temperature field in a jet engine model combustor segment with high pressure. In addition, Bohlin and Kliewer [20] recently developed a 2-D-CARS technique that enables planar temperature and chemical imaging in a combusting flow within a single laser pulse. However, PLIF and 2-D-CARS techniques require not only sophisticated and high-power laser sources but also accurate alignments of the laser beams that are generally realized by elaborate optics layouts. The combustors should be significantly modified to achieve two axis or through optical accesses that withstand the pressure rise and temperature of the combustion process. These requirements often make them less applicable for *in situ* and real-time monitoring of practical combustors that are operated in harsh environments, e.g., with dust and strong mechanical vibration.

With the rapid development of room-temperature and narrow-linewidth laser diodes, TDLAS techniques have been widely used for *in situ* and real-time combustion diagnosis [15], [21], [22]. By combining TDLAS with the tomographic concept, it becomes possible to measure spatially resolved 2-D distributions of temperature and species concentrations [23]–[25]. Particularly, a TDLAS tomographic sensor with good spatial resolution significantly benefits the understanding of heat release in swirling flames and reaction progress in such combustors. To improve the spatial resolution of TDLAS tomography, many efforts have been made to optimize the geometrical arrangements of the laser beams according to the structure of the combustion chamber [26]–[28]. Recently, sensors with optimized beam arrangements were applied to image continuously the hydrocarbon fuel distribution and mixing in both multicylinder and single-cylinder automotive engines [29], [30]. In addition, the so-called frequency-agile tomography method seeks to improve the spectral sampling through broadband wavelength sweeping for the alleviation of deficiencies in spatial sampling [31], [32]. However, the spatial resolution of such tomographic sensors should be further improved to meet the measurement requirements for capturing accurate temperature distribution and inferring the thermal expansion in the swirling flame. Recently, we developed a fan-beam TDLAS tomographic sensor with a spatial resolution of 7.8 mm in an imaged subject of diameter 60 mm, which has been proved to reconstruct accurate and stable 2-D distributions of temperature and H_2O concentration [33]. The applicability of the sensor to real-time flame monitoring was experimentally demonstrated on a flat-flame burner. The performance of the sensor makes it very promising for online monitoring of swirling flames. The developed sensor reported here is currently suitable for monitoring unconfined flames with unlimited optical access. By utilizing fiber optics to launch and collect thin pencil beams in the region of interest (ROI), the optical windows can be made very small and discontinuous around the perimeter of the combustor, in any arrangement that complies with the operational requirements of the combustor [29]. In this way, a TDLAS tomographic sensor can be further designed and embedded in practical combustors with minimal intrusions for monitoring confined swirling flames.

The current research aims at monitoring the dynamic cross-sectional behavior of swirling flames using the newly developed TDLAS tomographic system. The highly spatially resolved tomographic system was applied to monitor and reveal directly the reaction process of an unconfined swirling flame by reconstructing the 2-D distributions of temperature and H_2O concentration over the cross section of interest in the flame. In partially premixed combustion mode, accurate temperature distribution was captured to infer the thermal expansion of the swirling flame. In addition, thermal oscillations were extracted from the real-time 2-D reconstructions and used to indicate the instability of the swirling flame. To provide firsthand and reliable visual data that help prevent the flame from LBO, the developed system was further applied to capture the dynamic process of blowout of the unconfined swirling flame.

II. Physical and Mathematical Background of TDLAS Tomography

According to Beer's law, when a collimated laser beam of frequency υ [cm^{-1}] enters a flame with the thickness L [cm], the absorbance α_υ is expressed as

$$\alpha_\upsilon = \int_0^L P(x)X(x)S[T(x)]\phi dl \tag{1}$$

where $P(x)$ [atm] is the local total pressure, $X(x)$ is the local molar fraction of the absorbing species (noted as gas concentration hereafter), $T(x)$ [K] is the local temperature, and ϕ [cm] is the line shape function. The line strength of the transition $S[T(x)]$ [$\mathrm{cm}^{-2}\cdot\mathrm{atm}^{-1}$] is a function of temperature as follows:

$$S(T) = S(T_0)\frac{Q(T_0)}{Q(T)}\left(\frac{T_0}{T}\right)\exp\left[-\frac{hcE''}{k}\left(\frac{1}{T}-\frac{1}{T_0}\right)\right] \times \frac{1-\exp\left(-hc\upsilon_0/kT\right)}{1-\exp\left(-hc\upsilon_0/kT_0\right)} \tag{2}$$

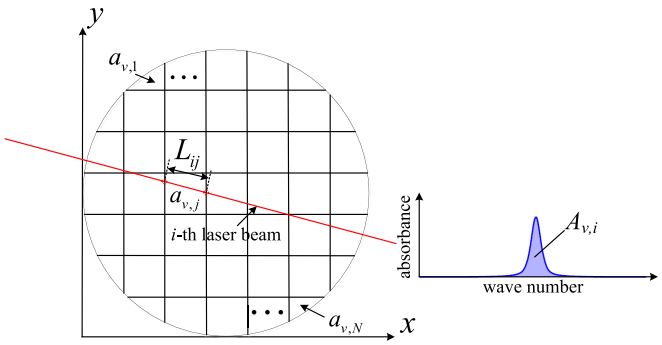

Fig. 1. Geometric description of a line-of-sight TDLAS measurement.

where h [J · s] is Planck's constant, c [cm · s^{-1}] is the speed of light, k [J · K^{-1}] is Boltzmann's constant, $Q(T)$ is the partition function of the absorbing molecule, T_0 [K] is the reference temperature, υ_0 [cm^{-1}] is the line-center frequency, and E'' [cm^{-1}] is the lower energy of the transition.

The line shape function ϕ is normalized so that $\int_{-\infty}^{+\infty} \phi d\upsilon \equiv 1$, so the integrated absorbance A_υ of the transition can be inferred from (1) as

$$A_\upsilon = \int_{-\infty}^{\infty} a_\upsilon d\upsilon = \int_0^L P(x)X_{abs}(x)S[T(x)]dl. \tag{3}$$

For the tomographic analysis, the circular ROI is discretized into N cells, as shown in Fig. 1. In the jth cell, P_j, T_j, and X_j are assumed to be constant. For the ith laser beam, the sampled integrated absorbance $A_{\upsilon,i}$, i.e., the projection, is expressed as

$$A_{\upsilon,i} = \sum_{j=1}^{N} a_{\upsilon,j}L_{ij} = \sum_{j=1}^{N} [PS(T)X]_{\upsilon,j}L_{ij} \tag{4}$$

where i and j are the indices of the laser beams and the cells, $a_{\upsilon,j}$ is the density of the integrated absorbance in the jth cell, and L_{ij} is the absorption path length of the ith laser beam within the jth cell.

For a total of M laser beams, $a_{\upsilon,j}$ can be retrieved using tomographic algorithms. By performing the tomographic reconstructions at two preselected transitions (υ_1 and υ_2) with different temperature dependences, the temperature T_j in the jth cell can be reconstructed from the ratio of the reconstructed $a_{\upsilon_1,j}$ and $a_{\upsilon_2,j}$ in the jth cell as follows:

$$T_j = \frac{hc}{k}\left(E_2'' - E_1''\right) \Bigg/ \left[\ln\frac{a_{\upsilon_1,j}}{a_{\upsilon_2,j}} + \ln\frac{S_2(T_0)}{S_1(T_0)} + \frac{hc}{k}\frac{\left(E_2'' - E_1''\right)}{T_0}\right]. \tag{5}$$

With T_j in hand, the concentration X_j can be simultaneously obtained from (4) at atmospheric pressure

$$X_j = a_{\upsilon_1,j}/S_1(T_j). \tag{6}$$

III. Experimental Arrangements

A. Experimental Platform for Swirl Combustion

Fig. 2 shows the schematic of the experimental platform for swirl combustion, which mainly includes the air/fuel supply systems, a plenum chamber, a model swirl injector, and an exhaust pipe.

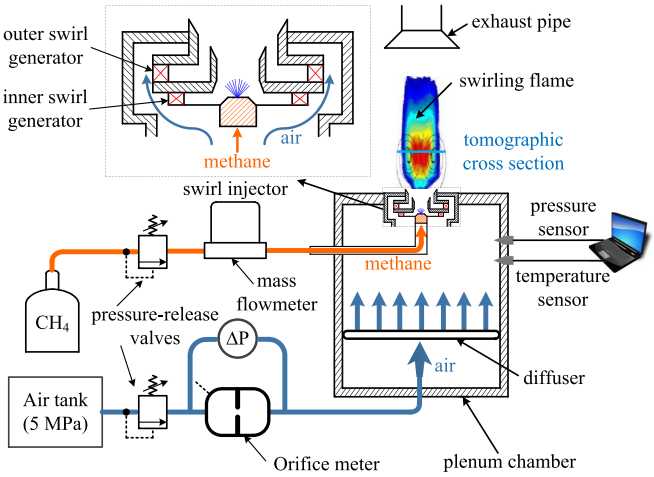

Fig. 2. Schematic of the experimental platform for swirl combustion.

In detail, a compressor was used to compress the air into a tank with pressure of 5 MPa. A pressure-release valve and an orifice meter were used to adjust and measure the air flow. The room-temperature air entered the plenum chamber and went through a diffuser. To maintain a stable working condition in the plenum chamber, the feedbacks obtained from the temperature and pressure sensors were used to control the pressure-release valve of the air supply system in real time. Then, the air with uniformly distributed flow passed two radial swirl generators, named as inner and outer swirl generators. The methane (CH_4) went through a pressure-release valve and its flow was precisely controlled using a mass flowmeter. The nonswirling methane was fed through the central nozzle and mixed with the swirled air from the inner swirl generator. Then, the mixed fuel was further mixed with the swirled air from the outer swirl generator and released from the 42-mm diameter nozzle of the swirl injector. To increase the shearing force of the flow, the inner and outer swirl generators swirled clockwise and anticlockwise, respectively. As a result, the mixing of air and methane was significantly enhanced, contributing to an efficient combustion process. After ignition, an unconfined swirling flame was formed above the nozzle of the model swirl injector. A conical top plate with a central exhaust tube formed the exit for the unburnt fuel and combustion products.

B. Measurement System

Fig. 3 shows a schematic of the online and high spatial resolution monitoring system for the swirling flames. The system mainly includes two distributed feedback (DFB) laser diodes and corresponding laser control modules, a stationary TDLAS tomographic sensor, a multichannel data acquisition system, and a host computer.

As a major product of the combustion of hydrocarbons, H_2O was selected as the target absorbing species. The central frequencies of the two DFB laser diodes were selected at 7444.36 cm^{-1} (NTT Electronics Corporation, NLK1B5GAAA) and 7185.6 cm^{-1} (NTT Electronics Corporation, NLK1E5GAAA), because of the moderate line strengths

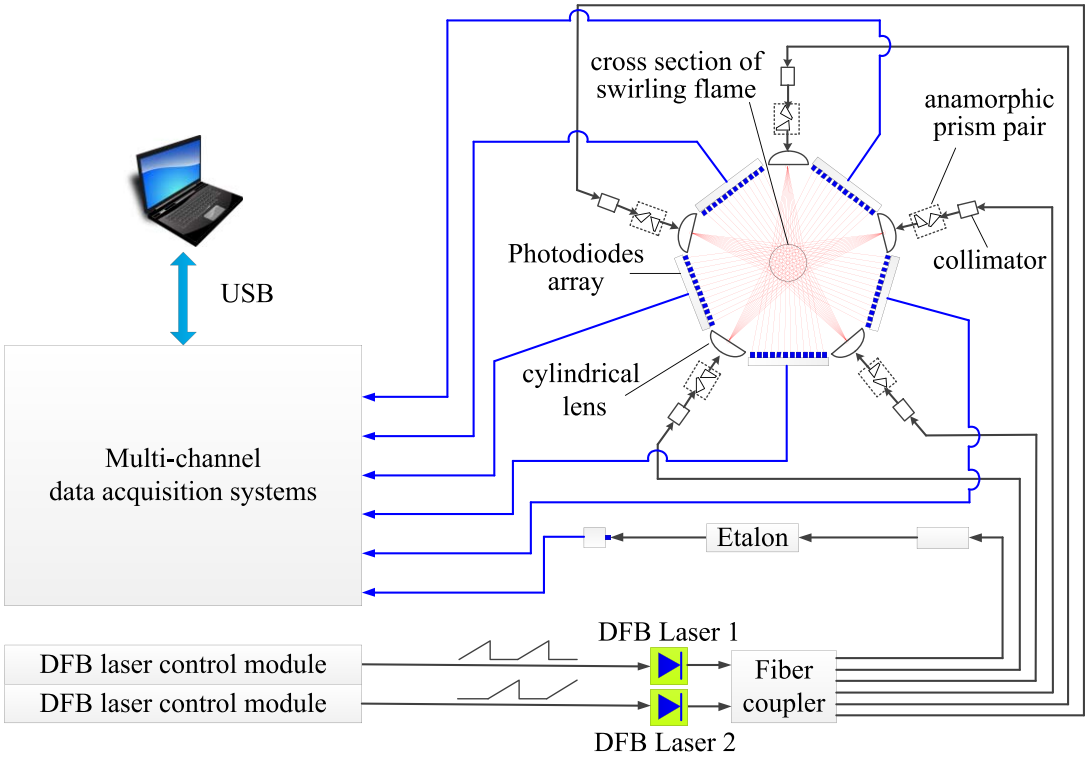

Fig. 3. Schematic of the TDLAS tomographic system.

and good temperature sensitivity of H_2O transitions at these two frequencies [33], [34]. The linewidth and maximum output power of the DFB laser diodes are 2 MHz and 20 mW, respectively. As the upper limit of the wavelength scanning speed of the DFB laser diode adopted in this work was 10 kHz, a temporal resolution of 0.2 ms could be realized with the time division multiplexing (TDM) scheme between the two laser diodes, corresponding to an imaging rate of 5 kHz or 5000 frames per second. The TDM scheme was realized using the developed DFB laser control modules and the control strategy detailed in [25] and [34]. The temporal resolution can be further improved when adopting a frequency-agile laser with a higher wavelength scanning speed. The output laser beams from the DFB laser diodes were combined using a fiber coupler and then split into six single-mode fibers with equal power. The laser beam output from one of the fibers penetrates an etalon with a free spectral range of 0.084 cm^{-1} to monitor the frequency during the wavelength scanning, while the other laser beams from the remaining fibers were connected to the newly developed TDLAS tomographic sensor to generate coplanar fan-beam illumination at five views.

The laser beam from each of the five optic fibers was first collimated and then guided through a combination of an anamorphic prism pair and a cylindrical lens [33]. In this way, the fan-beam illuminations with a span angle of 24° were simultaneously generated, which effectively covered the ROI with a diameter of 6 cm. The center of the ROI was located at the center of the target cross section of the swirling flame. Then, each fan-beam illumination penetrated the ROI, i.e., the cross section of interest in the swirling flame, and was sampled by a multiphotodiode array that contains 12 equally spaced photodiodes (G12180-010A, Hamamatsu). The spectral response range of the photodiode is from 0.9 to 1.7 μm with the peak sensitivity wavelength λ_p at 1.55 μm, while the typical photosensitivity at λ_p is 1.1 A/W.

As shown in Fig. 4(a), the sampled data were transferred in serial order of the beams ($i = 1, 2, \ldots, 60$) to the computer in real time, taking 12 ms per frame of 60-channel measurements. The data in each channel contain the absorption spectra of the transitions at 7185.6 and 7444.36 cm^{-1}. The absorbances were extracted from fitting the baseline of the transmitted laser intensity I_t. Then, the integrated absorbance values for both transitions $A_{v_1,i}$ and $A_{v_2,i}$ ($i = 1, 2, \ldots, 60$) were calculated from fitting the absorbances with Voigt line shape functions [35]. Fig. 4(b)–(d) shows the extracted absorbances from Fig. 4(a) and their Voigt fitting results with $i = 1, 2$, and 60, respectively. Finally, the integrated absorbance values were input to the modified Landweber algorithm to reconstruct the 2-D distributions of temperature and H_2O concentration [33], [36].

In addition, the spatial resolution of the designed TDLAS tomographic sensor using fan-beam illumination is 7.8 mm. Due to the use of the fan-beam method of illumination in this system and the relatively large number of measured "beams" (60) using the photodiode arrays, the spatial resolution of the present sensor is significantly better than that which could be achieved by using parallel-beam illumination and consequently many fewer beams for a 60-mm diameter subject. Moreover, the many illumination angles provided by the present sensor ensure that the angular sampling of the subject is well balanced

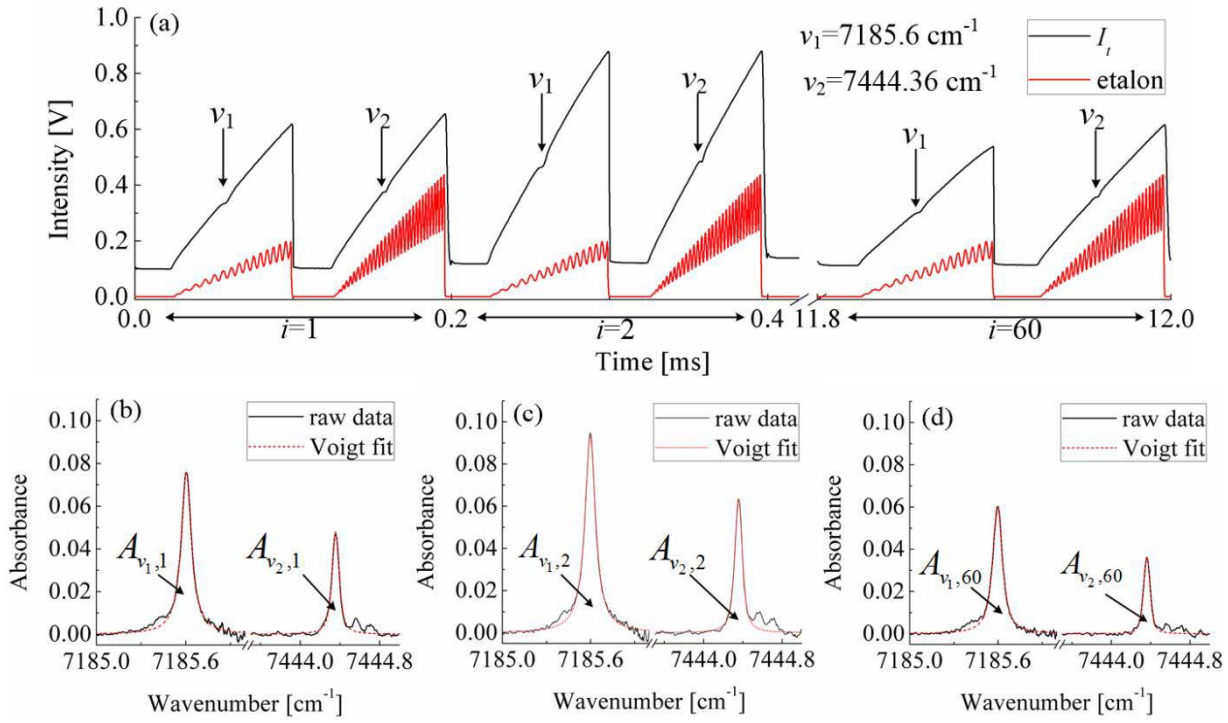

Fig. 4. Signal processing of the sampled TDLAS data. (a) Sampled data from 60 photodiodes for one frame of tomographic image. (b) Extracted absorbances from (a) and their Voigt fitting results for $i = 1$. (c) Similarly, for $i = 2$, and (d) for $i = 60$.

with the translational sampling relative to the subject center, thus minimizing artifacts in the tomographic images. As a result, more details of the swirling flame, such as accurate cross-sectional temperature profiles and thermal expansion, can be captured with the designed sensor. As shown in Fig. 5, five height-adjustable supports were used to image the cross sections of the swirling flame at various desired heights above the nozzle.

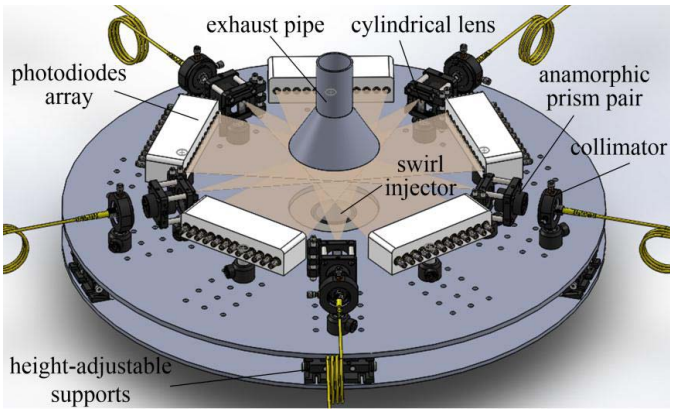

Fig. 5. Installation of the stationary TDLAS tomographic sensor above the nozzle of the model swirl injector.

IV. Results and Discussion

A. Cross-Sectional Images and On-Line Monitoring of Swirling Flame

In the experiment, the equivalence ratio of 0.205 is obtained by setting the flows of methane and air as 8 and 371 L/min, respectively. With the above settings, a stable swirling flame was generated above the nozzle of the model swirl injector after ignition. To balance the spatial resolution against the accuracy of the tomographic image, the radius of the ROI was set as 3 cm, while the cell size along both the directions of x- and y-axes was set as 0.3 cm [33]. The height above the nozzle of the swirl injector is denoted as z. The height of the fan-beam illumination was adjusted to 2 cm above the nozzle, that is, the cross section of interest in the swirling flame at $z = 2$ cm was selected as the target ROI.

To capture the dynamics of the swirling flame, instantaneous (i.e., single frame) distributions of temperature and H_2O concentration over the cross section at $z = 2$ cm were continuously reconstructed using the TDLAS tomographic system. In consideration of the continuous distributions of the temperature and H_2O concentration in the flame, a Gaussian low-pass filter of size 3×3 with a standard deviation of Gaussian distribution σ of 0.5 was applied within each iteration in the modified Landweber algorithm to remove the artifacts and render the inherently ill-posed problem more tractable. Fig. 6 shows three instantaneous tomographic images of (a)–(c) temperature and (d)–(f) H_2O concentration at time intervals of 12 ms, respectively. It can be seen that a crescent-shaped region rotates anticlockwise during the sequence of three tomographic images. The values of temperature and H_2O concentration in the crescent-shaped region are higher than those in the other regions of the ROI. In this case, the values of temperature and H_2O concentration in the crescent-shaped region are around 1750 K and 0.16, respectively.

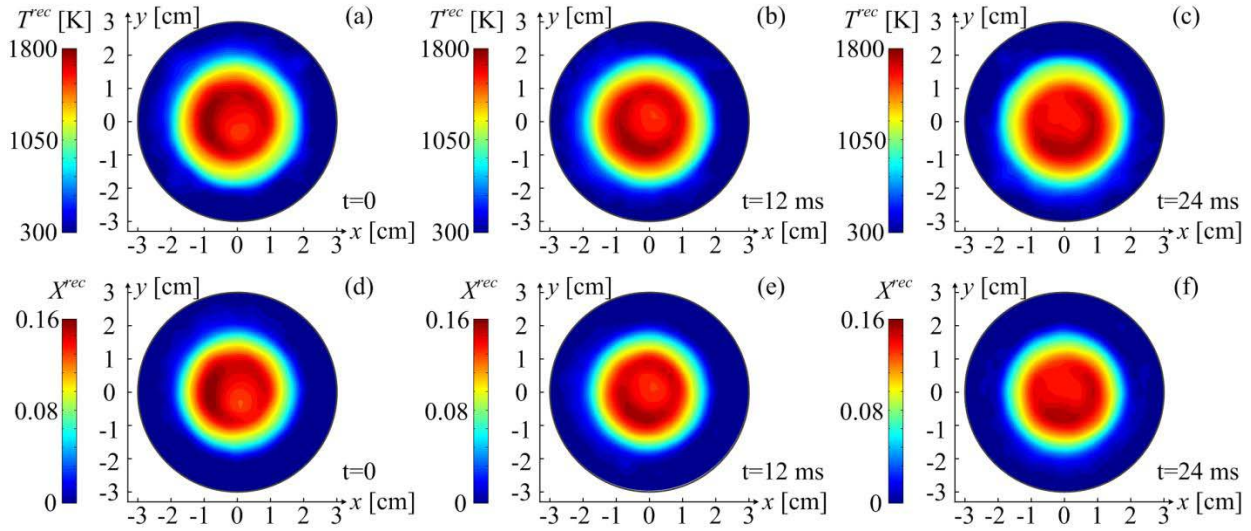

Fig. 6. Instantaneous tomographic images of (a)–(c) temperature and (d)–(f) H_2O concentration over the cross section of interest in the swirling flame at $z = 2$ cm when the flows of methane and air are 8 and 371 L/min, respectively. The time interval between the neighboring images of (a)–(c) temperature and (d)–(f) H_2O concentration is 12 ms.

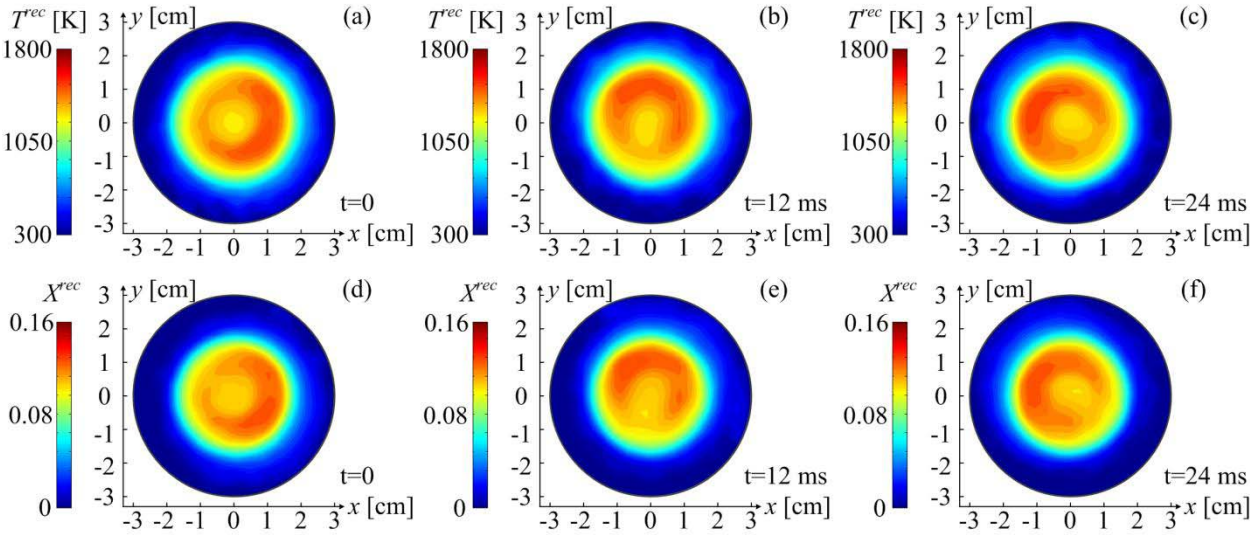

Fig. 7. Instantaneous tomographic images of (a)–(c) temperature and (d)–(f) H_2O concentration over the cross section of interest in the swirling flame at $z = 4$ cm when the flows of methane and air are 8 and 371 L/min, respectively. The time interval between the neighboring images of (a)–(c) temperature and (d)–(f) H_2O concentration is 12 ms.

The crescent-shaped region is formed by the cone-shaped spiral nature of the swirling flow [37]. The methane fed through the central nozzle is eventually swirled out into the co-swirling air. The interaction between the flow field and chemistry becomes significant in reacting flows due to the existence of vortex breakdown that induces flow recirculation [38]. The upstream recirculation zone is close to the swirling inlet, while the downstream recirculation zone is located in the central area. Strong velocity gradients occur in the inner side of the upstream recirculation zone, resulting in vortex breakdown that is generally aligned with the heat release. Therefore, a crescent-shaped region with high temperature values is observed over the cross section of the swirling flame. The sense of rotation of the crescent-shaped region is determined by the rotation of the whole spiral, which is anticlockwise in our case.

Then, the fan-beam illuminations were mounted at the height of 4 cm above the nozzle, i.e., $z = 4$ cm. In this way, the distributions of temperature and H_2O concentration over the cross section of interest in the swirling flame at $z = 4$ cm were reconstructed in real time. As shown in Fig. 7, there are still instantaneous crescent-shaped regions that rotate anticlockwise in the ROI. Compared with those at $z = 2$ cm, the crescent-shaped regions at $z = 4$ cm deviate a little from the center of the flame. The values of temperature and H_2O concentration in the crescent-shaped region are around 1400 K and 0.12, respectively. As the heat dissipates downstream of the nozzle, the temperature decreases as the height above

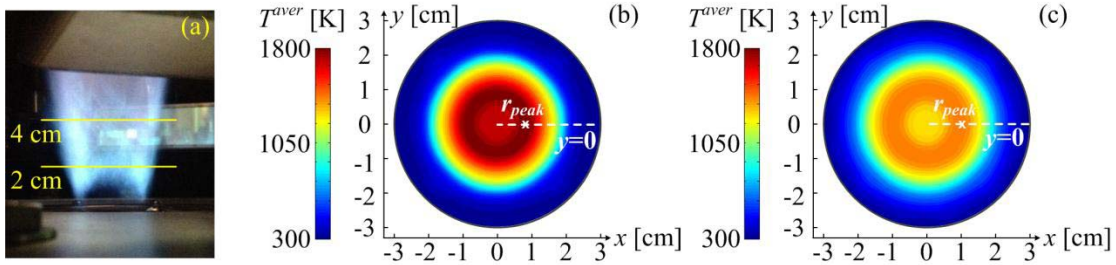

Fig. 8. (a) Photograph and averaged tomographic images of temperature over the cross section of interest in the swirling flame at (b) $z = 2$ cm and (c) $z = 4$ cm when the flows of methane and air are 8 and 371 L/min, respectively.

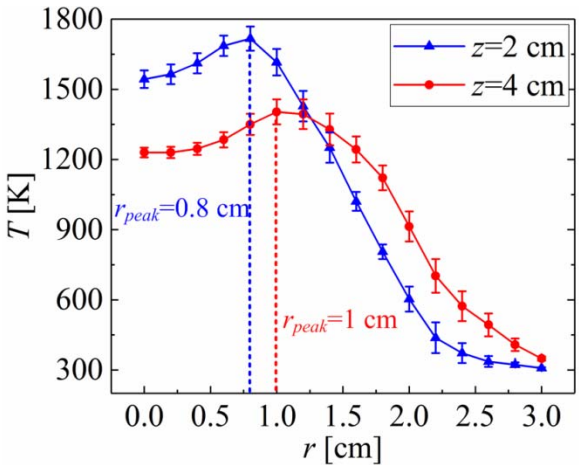

Fig. 9. Radial distributions of average temperature with its standard deviation over the cross section of the swirling flame at $z = 2$ cm and $z = 4$ cm when the flows of methane and air are 8 and 371 L/min, respectively.

the nozzle increases. In addition, H_2O concentration also decreases due to the expansion of the cross-sectional area of the swirling flame as it travels further away from the nozzle.

To highlight the mean temperature distribution of the swirling flame, 200 continuously reconstructed temperature distributions (corresponding to 2.4 s in real time) are averaged. In this way, the crescent-shaped regions in the radial dimension at different heights above the nozzle can be quantitatively located without external perturbations. Fig. 8(a)–(c) shows a photograph of the swirling flame and averaged tomographic images of temperature at $z = 2$ cm and $z = 4$ cm, respectively. It can be seen that the radius of the flame over the cross section at $z = 4$ cm is larger than that at $z = 2$ cm. In addition, the temperature distributions in the averaged images are rotationally symmetric. That is to say, the mean temperature values extracted from the same radius of the ROI are identical [34], [39], [40]. Here, mean temperature values on the positive x-axis in Fig. 8 are obtained. As shown in Fig. 9, the midpoints signify the mean temperature values, while the error bar to each midpoint denotes the standard deviation of the 200 solutions. The mean temperature values first increase from the flame center to the maximum value along the radius and then gradually decrease toward the boundary of the swirling flame. The radial distance between the peak of the temperature profile and the flame center is noted as r_{peak}. For $z = 2$ cm and $z = 4$ cm, r_{peak} is 0.8 and 1 cm, respectively. It can be deduced that the flame swirled in an anticlockwise helical route with a radial expansion of 0.2 cm from $z = 2$ cm to $z = 4$ cm. Due to the rotation of the high-temperature crescent-shaped regions, the standard deviations around the peak are larger than those in the center and on the boundary of the swirling flame.

TABLE I
EXPERIMENTAL CONDITIONS WITH DIFFERENT FLOW RATES AND EQUIVALENCE RATIOS

Flow rates (L/min)		Equivalence ratio
air	methane	
371	8	0.205
371	6	0.153
371	4	0.101

B. Cross-Sectional Monitoring of Swirling Flame Close to Lean Blowout Limit

As the equivalence ratio decreases, the swirling flame will be closer to the LBO limit. The objectives to reliably determine the proximity to LBO during operation, and better understand the dynamics of the swirling flame near the LBO limit, motivate a desire for online monitoring of the swirling flame with decreasing equivalence ratios. In the experiments, the 2-D distributions of temperature and H_2O concentration over the cross section of interest in the swirling flame were reconstructed in real time as the equivalence ratio decreased. As shown in Table I, the equivalence ratio was decreased from 0.205 to 0.101 when the air flow was kept unchanged at 371 L/min and the methane flow was decreased from 8 to 4 L/min.

Fig. 10 shows a sequence of instantaneous tomographic images of temperature at the height of 2 cm above the nozzle when the methane flows are 6 and 4 L/min, respectively. In this experiment, a crescent-shaped region that rotated anticlockwise over the cross section was observed, similar to that observed in Fig. 6. In comparison with the reconstructed results in Fig. 6, the maximum temperature values in the crescent-shaped region decrease to around 1450 and 1030 K when the methane flows are 6 and 4 L/min, respectively. The swirling flame is still stabilized with the rotation of the helical structure around the central axis.

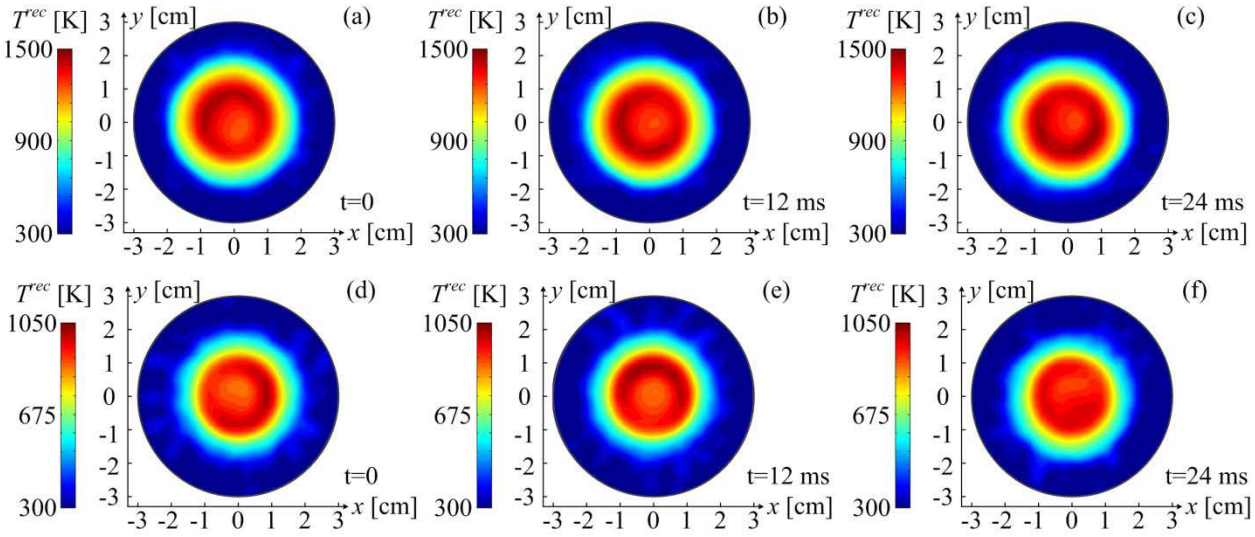

Fig. 10. Instantaneous tomographic images of temperature over the cross section of interest in the swirling flame at $z = 2$ cm when the air flow is 371 L/min and the methane flows are (a)–(c) 6 and (d)–(f) 4 L/min, respectively. The time interval between the neighboring images is 12 ms.

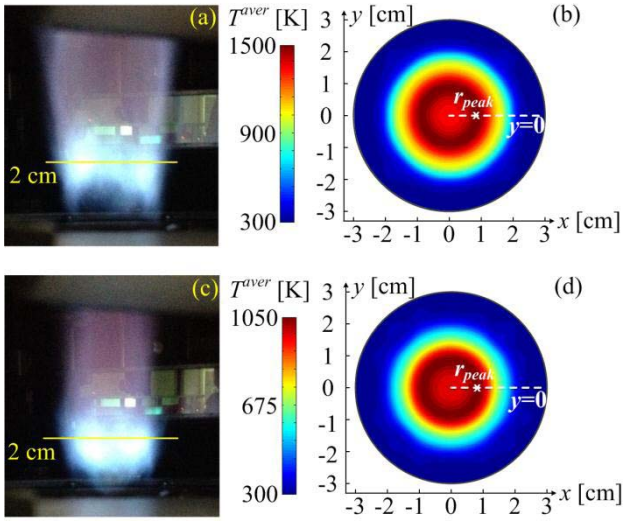

Fig. 11. Photographs and averaged tomographic images of temperature over the cross section of interest in the swirling flame at $z = 2$ cm with the air flow being set as 371 L/min and the methane flows being set as (a) and (b) 6 L/min and (c) and (d) 4 L/min, respectively.

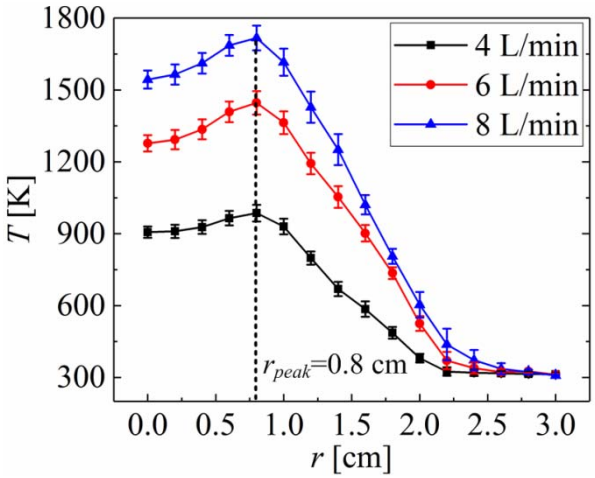

Fig. 12. Radial distributions of average temperature with its standard deviation over the cross section of interest in the swirling flame at $z = 2$ cm when the air flow is 371 L/min and the methane flows are 8, 6, and 4 L/min, respectively.

Two hundred continuously reconstructed temperature distributions as exemplified in Fig. 10 were averaged to analyze the dependence of the thermal distribution in the swirling flame on the decreasing methane flow. As shown in Fig. 11, the photographs and the average temperature distributions are rotationally symmetric for both cases. The mean temperature values were also extracted from the positive x-axis in each averaged image. Fig. 12 shows the radial distributions of mean temperature values with its standard deviations of the 200 solutions over the cross section of the swirling flame at $z = 2$ cm when the methane flows are 8, 6, and 4 L/min, respectively. It can be seen that the temperature of the swirling flame decreases as the methane flow decreases. The expansion of the flow field is mainly determined by the structure of the swirlers and the initial jet flow. In these three cases, the air flow, i.e., 371 L/min, is much larger than the methane flows, resulting in the similar jet flows. That is to say, the extent of flow expansion close to the nozzle of the swirl injector is similar for all three cases. Therefore, the crescent-shaped regions rotate with the similar radius when the methane flows are 8, 6, and 4 L/min, while the peak values of the temperature profiles for all three cases are located at $r = 0.8$ cm.

Fig. 13 shows the time-resolved temperature values at the coordinate (r_{peak}, 0) over the cross sections at $z = 2$ cm and the corresponding spectral analysis results when the air flow is 371 L/min and the methane flows are 8, 6, and 4 L/min, respectively. To clearly identify thermal oscillation, the fast Fourier transform was applied to the time-resolved temperature values. It should be noted that the point on the coordinate (r_{peak}, 0) is

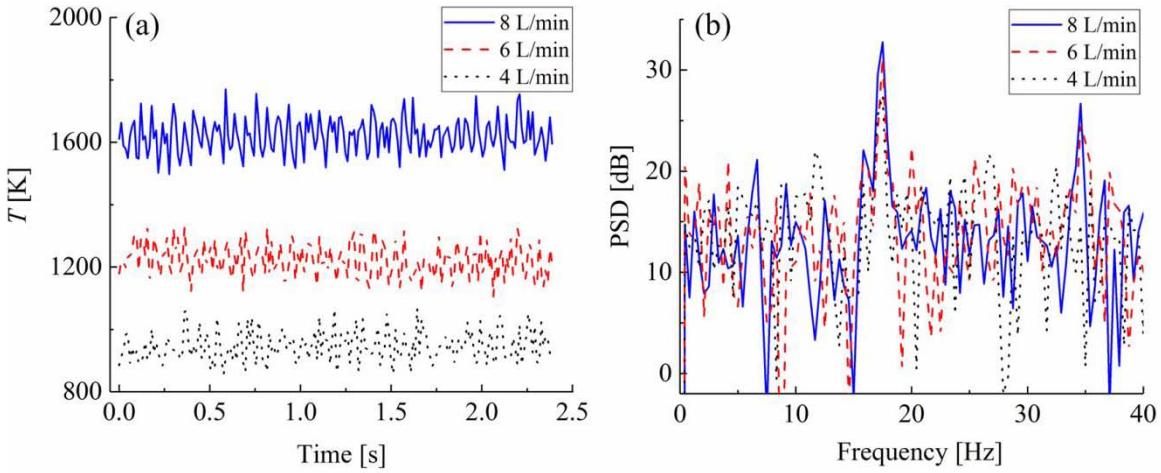

Fig. 13. Analysis of the thermal oscillations of the swirling flame over the cross section at $z = 2$ cm with decreasing equivalence ratio. (a) Temperature values at (r_{peak}, 0) obtained from the 200 continuously reconstructed temperature distributions when the air flow is 371 L/min and the methane flows are 8 L/min (solid curve), 6 L/min (dashed curve), and 4 L/min (dotted curve). (b) Power spectra of the root-mean-square temperature values in (a).

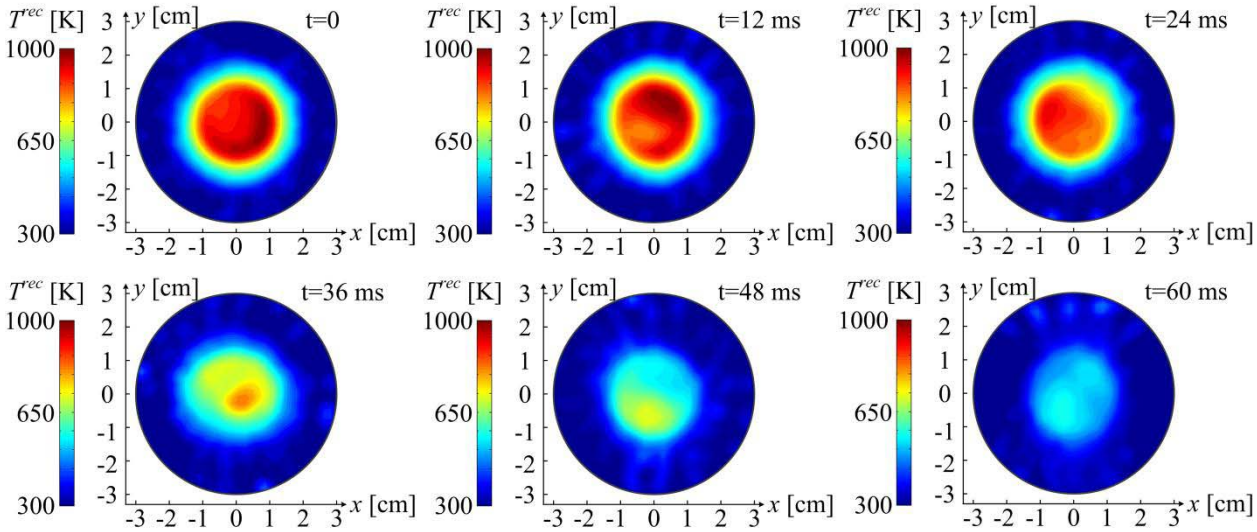

Fig. 14. Instantaneous tomographic images of temperature over the cross section of the swirling flame at $z = 2$ cm during the blowout event. The time interval between the neighboring images of temperature is 12 ms.

selected for spectral analysis by taking both the signature of oscillation and noise effect into consideration. As the temperature gradient in the central recirculation area is relatively small, the flame oscillation can hardly be identified at the point in the center of the ROI. The temperature measurement at the point close to the boundary of the ROI will be contaminated with noises caused by violent gas convection at the flame boundary. Furthermore, the spectral analysis based on the oscillation-sensitive point is superior to that based on a line-of-sight TDLAS sensor, by which the path-integrated measurement result obtained from regions oscillating at different phases may reduce the observed strength of oscillation. In the three cases, the temperature oscillates with a main frequency of 17.5 Hz at the coordinate (r_{peak}, 0). The amplitude of thermal oscillation shown in Fig. 13(a) reduces when the equivalence ratio is decreased and thus yields a lower peak in the power spectral densities shown in Fig. 13(b). As unsteady heat release is coupled with the swirling flame, additional power leaks out to frequencies other than the main oscillation frequency. When the equivalence ratio is decreased, the swirling flame comes closer to the LBO and suffers from unsteady heat release to a larger extent. Therefore, the amplitude of the leaked power to frequencies other than the main oscillation frequency increases when the equivalence ratio is decreased.

When the methane flow was further decreased from 4 L/min, the blowout event occurred. To dynamically monitor the flame during the blowout event, a sequence of instantaneous temperature distributions at $z = 2$ cm were reconstructed in real time as the methane flow was decreased. As shown in Fig. 14, the crescent-shaped regions can still be seen in the tomographic images at $t = 0$ and $t = 12$ ms during the blowout event. Due to the decreased equivalence ratio, the temperature of the central recirculation zone was too low to ignite the fuel releasing from the nozzle of the swirl injector.

That is to say, the supply of heat from the flame root cannot stabilize the swirling flame any more [6]. It can be seen from the tomographic image at $t = 24$ ms that the blowout event started with the deformation of the crescent-shaped region, which may be caused by the inability to ignite the flame root. Then, the crescent-shaped region completely disappeared from $t = 36$ ms, denoting that the rotation of the helical structure around the central axis can no longer be sustained. With the disappearance of the rotationally crescent-shaped region, the flame rapidly blew out. It can be concluded that the developed TDLAS tomography system is capable of capturing the dynamic temperature profiles of the swirling flame during the blowout event. In practical applications, the online monitoring results can be used to investigate the LBO mechanism as the equivalence ratio is reduced and provide reliable parameters for LBO control strategies. In addition, the measurement results can also provide feedbacks to improve the structure of the swirl injectors and enhance their performance.

V. Conclusion

The newly developed TDLAS tomographic system was applied to monitor in real time the dynamic behavior and properties of a swirling flame. The 2-D distributions of temperature and H_2O concentration over the cross section of interest in the swirling flame were reconstructed in real time. In partially premixed combustion mode, the instantaneous images obtained from the TDLAS tomographic sensor with excellent spatial resolution of 7.8 mm enabled retrieval of the crescent-shaped region within the ROI that were used to infer the thermal distribution in the swirling flame. With the model swirl injector, the measurement results showed that the crescent-shaped region went upward in an anticlockwise helical route and gradually deviated from the center of the swirling flame.

With a fixed air flow of 371 L/min, decreased methane flow caused decrease of temperature in the swirling flame. In the case of stabilized swirling combustion, the crescent-shaped regions rotated around the same radius in the ROI as the methane flow decreased from 8 to 4 L/min. As known from the spectral analysis of the time-resolved thermal oscillations, the swirling flame suffers from unsteady heat release to a larger extent when the equivalence ratio is decreased to around 0.1 and thus causes the swirling flame to approach the LBO limit.

Dynamic temperature profiles of the swirling flame during the blowout event were successfully captured by the developed system. The blowout started from deformation of the crescent-shaped region in the ROI. As the rotation of this helical structure could no longer be sustained, the crescent-shaped region completely disappeared and the flame finally blew out. The cross-sectional dynamic behavior of the swirling flame reported here has been observed experimentally for the first time, due to the imaging capability, both in spatial and temporal resolutions, of the TDLAS tomography system.

Acknowledgment

The authors would like to thank Prof. M. Linne for his useful suggestions.

References

[1] "Global emissions," Int. Civil Aviation Org. (ICAO) Environ. Rep. 2016, Aviation Climate Change, Tech. Rep., 2016, ch. 4. [Online]. Available: https://www.icao.int/environmental-protection/Pages/env2016.aspx

[2] Y. Huang and V. Yang, "Dynamics and stability of lean-premixed swirl-stabilized combustion," *Prog. Energy Combustion Sci.*, vol. 35, no. 4, pp. 293–364, 2009.

[3] C. H. Cho, G. M. Baek, C. H. Sohn, J. H. Cho, and H. S. Kim, "A numerical approach to reduction of NO_x emission from swirl premix burner in a gas turbine combustor," *Appl. Therm. Eng.*, vol. 59, nos. 1–2, pp. 454–463, 2013.

[4] H.-G. Sung, "Combustion dynamics in a model lean-premixed gas turbine with a swirl stabilized injector," *J. Mech. Sci. Technol.*, vol. 21, pp. 495–504, Mar. 2007.

[5] R. Santhosh and S. Basu, "Transitions and blowoff of unconfined non-premixed swirling flame," *Combustion Flame*, vol. 164, pp. 35–52, Feb. 2016.

[6] M. Stöhr, I. Boxx, C. Carter, and W. Meier, "Dynamics of lean blowout of a swirl-stabilized flame in a gas turbine model combustor," *Proc. Combustion Inst.*, vol. 33, no. 2, pp. 2953–2960, 2011.

[7] M. G. De Giorgi *et al.*, "Lean blowout sensing and plasma actuation of non-premixed flames," *IEEE Sensors J.*, vol. 16, no. 10, pp. 3896–3903, May 2016.

[8] M. Thiruchengode *et al.*, "An active control system for LBO margin reduction in turbine engines," in *Proc. 41st Aeros. Sci. Meeting Exhib.*, 2003, p. AIAA 2003-1008.

[9] Y. Deguchi *et al.*, "Industrial applications of temperature and species concentration monitoring using laser diagnostics," *Meas. Sci. Technol.*, vol. 13, no. 10, pp. R103–R115, 2002.

[10] R. S. Das and Y. K. Agrawal, "Raman spectroscopy: Recent advancements, techniques and applications," *Vibrat. Spectrosc.*, vol. 57, no. 2, pp. 163–176, 2011.

[11] S. Roy, J. R. Gord, and A. K. Patnaik, "Recent advances in coherent anti-Stokes Raman scattering spectroscopy: Fundamental developments and applications in reacting flows," *Prog. Energy Combustion Sci.*, vol. 36, no. 2, pp. 280–306, 2010.

[12] M. P. Thariyan, A. H. Bhuiyan, S. E. Meyer, S. V. Naik, J. P. Gore, and R. P. Lucht, "Dual-pump coherent anti-Stokes Raman scattering system for temperature and species measurements in an optically accessible high-pressure gas turbine combustor facility," *Meas. Sci. Technol.*, vol. 22, no. 1, pp. 015301-1–015301-12, 2011.

[13] C. Schulz and V. Sick, "Tracer-LIF diagnostics: Quantitative measurement of fuel concentration, temperature and fuel/air ratio in practical combustion systems," *Prog. Energy Combustion Sci.*, vol. 31, no. 1, pp. 75–121, 2005.

[14] D. R. Richardson, N. Jiang, D. L. Blunck, J. R. Gord, and S. Roy, "Characterization of inverse diffusion flames in vitiated cross flows via two-photon planar laser-induced fluorescence of CO and 2-D thermometry," *Combustion Flame*, vol. 168, pp. 270–285, Jun. 2016.

[15] M. A. Bolshov, Y. A. Kuritsyn, and Y. V. Romanovskii, "Tunable diode laser spectroscopy as a technique for combustion diagnostics," *Spectrochimica Acta B, Atomic Spectrosc.*, vol. 106, pp. 45–66, Apr. 2015.

[16] C. S. Goldenstein, R. M. Spearrin, J. B. Jeffries, and R. K. Hanson, "Infrared laser-absorption sensing for combustion gases," *Prog. Energy Combustion Sci.*, vol. 60, pp. 132–176, May 2017.

[17] H. Li, X. Zhou, J. B. Jeffries, and R. K. Hanson, "Sensing and control of combustion instabilities in swirl-stabilized combustors using diode-laser absorption," *AIAA J.*, vol. 45, no. 2, pp. 390–398, 2007.

[18] U. Stopper *et al.*, "PIV, 2D-LIF and 1D-Raman measurements of flow field, composition and temperature in premixed gas turbine flames," *Experim. Therm. Fluid Sci.*, vol. 34, no. 3, pp. 396–403, 2010.

[19] U. E. Meier, D. Wolff-Gaßmann, and W. Stricker, "LIF imaging and 2D temperature mapping in a model combustor at elevated pressure," *Aerosp. Sci. Technol.*, vol. 4, no. 6, pp. 403–414, 2000.

[20] A. Bohlin and C. J. Kliewer, "Diagnostic imaging in flames with instantaneous planar coherent Raman spectroscopy," *J. Phys. Chem. Lett.*, vol. 5, no. 7, pp. 1243–1248, 2014.

[21] M. G. Allen, "Diode laser absorption sensors for gas-dynamic and combustion flows," *Meas. Sci. Technol.*, vol. 9, no. 4, pp. 545–562, 1998.

[22] R. M. Mihalcea, D. S. Baer, and R. K. Hanson, "A diode-laser absorption sensor system for combustion emission measurements," *Meas. Sci. Technol.*, vol. 9, no. 3, pp. 327–338, 1998.

[23] F. Wang *et al.*, "Two-dimensional tomography for gas concentration and temperature distributions based on tunable diode laser absorption spectroscopy," *Meas. Sci. Technol.*, vol. 21, no. 4, pp. 045301-1–045301-10, 2010.

[24] W. Cai and C. F. Kaminski, "Tomographic absorption spectroscopy for the study of gas dynamics and reactive flows," *Prog. Energy Combustion Sci.*, vol. 59, pp. 1–31, Mar. 2017.
[25] L. Xu, C. Liu, W. Jing, Z. Cao, X. Xue, and Y. Lin, "Tunable diode laser absorption spectroscopy-based tomography system for on-line monitoring of two-dimensional distributions of temperature and H_2O mole fraction," *Rev. Sci. Instrum.*, vol. 87, no. 1, p. 013101, 2016.
[26] S. A. Tsekenis *et al.*, "Towards in-cylinder chemical species tomography on large-bore IC engines with pre-chamber," *Flow Meas. Instrum.*, vol. 53, pp. 116–125, Mar. 2017.
[27] N. Terzija *et al.*, "Image optimization for chemical species tomography with an irregular and sparse beam array," *Meas. Sci. Technol.*, vol. 19, no. 9, pp. 094007-1–094007-13, 2008.
[28] S. J. Grauer, P. J. Hadwin, and K. J. Daun, "Bayesian approach to the design of chemical species tomography experiments," *Appl. Opt.*, vol. 55, no. 21, pp. 5772–5782, 2016.
[29] P. Wright *et al.*, "High-speed chemical species tomography in a multi-cylinder automotive engine," *Chem. Eng. J.*, vol. 158, no. 1, pp. 2–10, 2010.
[30] N. Terzija, S. Karagiannopoulos, S. Begg, P. Wright, K. Ozanyan, and H. McCann, "Tomographic imaging of the liquid and vapour fuel distributions in a single-cylinder direct-injection gasoline engine," *Int. J. Engine Res.*, vol. 16, no. 4, pp. 565–579, 2015.
[31] W. Cai and C. F. Kaminski, "A tomographic technique for the simultaneous imaging of temperature, chemical species, and pressure in reactive flows using absorption spectroscopy with frequency-agile lasers," *Appl. Phys. Lett.*, vol. 104, no. 3, p. 034101, 2014.
[32] L. Ma *et al.*, "50-kHz-rate 2D imaging of temperature and H_2O concentration at the exhaust plane of a J85 engine using hyperspectral tomography," *Opt. Exp.*, vol. 21, no. 1, pp. 1152–1162, 2013.
[33] C. Liu, L. Xu, J. Chen, Z. Cao, Y. Lin, and W. Cai, "Development of a fan-beam TDLAS-based tomographic sensor for rapid imaging of temperature and gas concentration," *Opt. Exp.*, vol. 23, no. 17, pp. 22494–22511, 2015.
[34] C. Liu, L. Xu, Z. Cao, and H. McCann, "Reconstruction of axisymmetric temperature and gas concentration distributions by combining fan-beam TDLAS with onion-peeling deconvolution," *IEEE Trans. Instrum. Meas.*, vol. 63, no. 12, pp. 3067–3075, Dec. 2014.
[35] L. Xu, C. Liu, D. Zheng, Z. Cao, and W. Cai, "Digital signal processor-based high-precision on-line Voigt lineshape fitting for direct absorption spectroscopy," *Rev. Sci. Instrum.*, vol. 85, no. 12, p. 123108, 2014.
[36] W. Q. Yang, D. M. Spink, T. A. York, and H. McCann, "An image-reconstruction algorithm based on Landweber's iteration method for electrical-capacitance tomography," *Meas. Sci. Technol.*, vol. 10, no. 11, pp. 1065–1069, 1999.
[37] Y. M. Al-Abdeli and A. R. Masri, "Recirculation and flowfield regimes of unconfined non-reacting swirling flows," *Experim. Therm. Fluid Sci.*, vol. 27, no. 5, pp. 655–665, 2003.
[38] N. Syred, "A review of oscillation mechanisms and the role of the precessing vortex core (PVC) in swirl combustion systems," *Prog. Energy Combustion Sci.*, vol. 32, no. 2, pp. 93–161, 2006.
[39] C. Liu, L. Xu, F. Li, Z. Cao, S. A. Tsekenis, and H. McCann, "Resolution-doubled one-dimensional wavelength modulation spectroscopy tomography for flame flatness validation of a flat-flame burner," *Appl. Phys. B, Lasers Opt.*, vol. 120, no. 3, pp. 407–416, 2015.
[40] C. Liu, Z. Cao, F. Li, Y. Lin, and L. Xu, "Flame monitoring of a model swirl injector using 1D tunable diode laser absorption spectroscopy tomography," *Meas. Sci. Technol.*, vol. 28, no. 5, pp. 054002-1–054002-8, 2017.

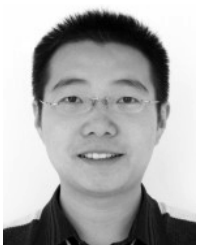

Chang Liu received the B.Sc. degree in automation from Tianjin University, Tianjin, China, in 2010, the Ph.D. degree in testing, measurement technology and instrument from Beihang University, Beijing, China, in 2016.

From 2016 to 2018, he was a Post-Doctoral Researcher with the Department of Air Pollution and Environmental Technology, Empa-Swiss Federal Laboratories for Materials Science and Technology, Dübendorf, Switzerland. Since 2018, he has been a Lecturer with the School of Engineering, The University of Edinburgh, Edinburgh, U.K. His current research interests include NIR/MIR laser absorption spectroscopy (LAS), LAS tomographic technique and system design, and their applications to combustion diagnostic and trace gas sensing.

Zhang Cao (M'10) received the B.Sc. degree (with distinction) in automation and the M.Eng. and Ph.D. degrees (with distinctions) in measurement technology and automatic devices from Tianjin University, Tianjin, China, in 2003, 2005, and 2008, respectively.

Since 2008, he has been with Beihang University, Beijing, China, where he is currently a Professor with the School of Instrumentation Science and Opto-Electronic Engineering. His current research interests include process tomography, multiphase flow measurement, and inverse problems.

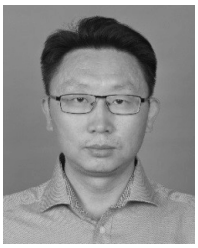

Yuzhen Lin received the B.Sc., M.Eng., and Ph.D. degrees in combustion of aircraft engine from Beihang University, Beijing, China, in 1991, 1994, and 1997, respectively.

He is currently a Full Professor with Beihang University. His current research interests include general area of gas turbine combustion, special emphasis on ultra-low emissions combustion, combustion instability, unsteady combustion physics, spray ignition, and autoignition. His teaching responsibility includes teaching undergraduate- and graduate-level combustion courses.

Lijun Xu (M'04–SM'04) received the B.Sc., M.Eng., and Ph.D. degrees in electrical engineering and instrumentation from Tianjin University, Tianjin, China, in 1990, 1993, and 1996, respectively.

From 1997 to 2001, he was an Associate Professor with Tianjin University. From 2002 to 2006, he was a Research Fellow with the University of Greenwich, London, U.K. and the University of Kent, Canterbury, U.K., and a Higher Scientific Officer with the Institute of Cancer Research, Sutton, U.K. He is currently a Professor with Beihang University, Beijing, China, where he is also the Dean of the School of Instrumentation Science and Opto-Electronic Engineering. He has authored or co-authored over 260 publications. His current research interests include tomographic imaging, scanning imaging, and dynamic process monitoring.

Dr. Xu received the National Science Fund for Distinguished Young Scholars in 2012. He was a recipient of the Ministry of Education Technology Invention Award (first class) in 2012 and the China Instrument Society Science and Technology Award (first class) in 2014. He was elected as Chang-Jiang Scholars Program Professor and National High-Level Personnel of the Special Support Program by the Ministry of Education and the Ministry of Organisation, China, in 2014 and 2016, respectively.

Hugh McCann received the B.Sc. and Ph.D. degrees from the University of Glasgow, Glasgow, U.K., in 1976 and 1980, respectively.

He was an appointed Professor of tomographic imaging and the Head of the School of Engineering, The University of Edinburgh, Edinburgh, U.K., in 2013. From 1996 to 2013, he was a Professor of industrial tomography with The University of Manchester, Manchester, U.K., following ten years in research and development with the Royal Dutch/Shell Group, The Hague, The Netherlands. He was involved in high-energy particle physics for ten years at Glasgow, Manchester, CERN, Geneva, Switzerland, and DESY, Hamburg, Germany. He has extended industrial tomography to provide specific chemical contrast using high-speed all-opto-electronic techniques, and has developed electrical impedance tomography for medical applications, collaborating intensively with users in both academia and industry. He was the Head of the School of Electrical and Electronic Engineering, Manchester, U.K., from 1999 to 2002, the Chair of U.K. Professors, and the Head of electrical engineering from 2003 to 2005 and the Virtual Centre for Industrial Process Tomography from 2005 to 2009.

Prof. McCann was elected as a fellow of the Royal Academy of Engineering in 2009 and the Royal Society of Edinburgh in 2015.